PAPER

Check for updates

Regenerated and reformed gold and titanium dioxide quantum dots from waste for sustainable and efficient environmental monitoring†

Zain Ul Abideen, [ID] * Rasoul Khayyam Nekouei, [ID] Mohsen Hajian Foroushani, Samane Maroufi, [ID] Farshid Pahlevani and Veena Sahajwalla

Driven by the urgent need for sustainable materials in advanced technologies, this study investigates the potential of regenerated and reformed waste materials containing Au and TiO_2 quantum dots (R-Au–TiO_2 QDs), derived from industrial waste, as a viable alternative to commercial TiO_2 (C-TiO_2) for photocatalytic applications. The R-Au–TiO_2 QDs demonstrate a high purity of 99.8 wt% and a particle size of less than 10 nm. The presence of Au (0.24 wt%) further enhances the photocatalytic performance of R-Au–TiO_2 QDs through localized surface plasmon resonance (LSPR), leading to superior degradation rates of methylene blue (MB) when deposited on flexible aluminum foil substrates under UV and solar light. R-Au–TiO_2 QDs achieve a degradation rate of 82.5% with a rate constant of 0.029 min^{-1} under UV light, representing a 28% increase in degradation rate and a 70% increase in the rate constant compared to 64.5% and 0.017 min^{-1}, respectively, for C-TiO_2. Under the solar simulator, R-Au–TiO_2 QDs also outperform C-TiO_2, achieving a degradation rate of 68%, further highlighting their effectiveness. These results are attributed to smaller particle size, higher surface area, enhanced light absorption and improved charge separation in the R-Au–TiO_2 hybrid material. This study demonstrates that R-Au–TiO_2 QDs not only match, but often surpass, the performance of commercial TiO_2, offering a cost-effective and environmentally friendly solution for UV sensing, environmental monitoring, and water purification systems. These findings advocate for the strategic utilization of waste resources containing valuable elements to regenerate high-performance materials, thereby contributing to the development of a circular and sustainable economy.

1. Introduction

The metallurgical industry is a significant contributor to industrial waste, generating vast amounts of by-products including slag, dust, and sludge from processes such as smelting, refining, and steel production.[1] Annually, this industry produces an estimated 400 million metric tons of waste, which, if not managed properly, poses severe environmental risks, including contamination of soil, water, and air, leading to ecological damage and health hazards.[1,2] Improper disposal of metallurgical waste, particularly through landfilling, can lead to the leaching of heavy metals such as lead, cadmium, and mercury into the environment, causing long-term contamination and health risks such as neurological disorders and cancer.[2,3] Moreover, this disposal method contributes to

biodiversity loss and ecosystem disruption. Recovering these materials conserves natural resources and minimizes the environmental impact associated with primary mining.[4,5]

Reforming metallurgical waste is both environmentally and economically advantageous, aligning with the objectives of Sustainable Development Goal 12 (SDG 12), which emphasizes sustainable consumption and production. SDG 12 focuses on optimizing resource use and minimizing the loss of energy and materials in the form of waste and emissions throughout the life cycle of products. In the metallurgical industry, this goal has garnered significant attention as companies seek to recover valuable metals from production waste, reduce energy consumption, and lower greenhouse gas emissions. By adopting circular economy practices, such as reforming and recycling slag, dust, and other metallurgical by-products, the industry not only mitigates environmental impact but also enhances resource efficiency, contributing to both economic sustainability and environmental stewardship.[6–8] Recent studies have also demonstrated the successful development of waste-derived catalysts and functional materials for energy and environmental applications, further supporting the value of

Centre for Sustainable Materials Research and Technology (SMaRT), School of Materials Science and Engineering, UNSW Sydney 2052, NSW, Australia.
E-mail: zain.abideen@unsw.edu.au

waste valorization strategies.[9,10] However, the complex composition of metallurgical waste, with its mix of valuable and hazardous components, makes the recovery process challenging. Therefore, we have suggested that these components should be used in a reformed state, going beyond conventional recycling.

Metallurgical waste is rich in different valuable metals such as gold (Au) and titanium dioxide (TiO_2), making it a critical resource for recovery.[2] For example, metallurgical slag can contain up to 84.5% TiO_2, essential for various industrial applications, including the production of pigments, coatings, and photocatalysts.[4] Au and TiO_2 are particularly valuable for applications in photocatalysis.[11] Au nanoparticles, known for their unique optical properties such as localized surface plasmon resonance (LSPR), enhance light absorption and are effective in biosensing, imaging, and catalysis.[12–14] On the other hand, TiO_2 is a widely studied semiconductor for its photocatalytic properties, stability, and non-toxicity, especially in environmental remediation. When exposed to light with energy equal to or greater than its bandgap (3.2 eV for anatase TiO_2), TiO_2 generates electron–hole pairs that drive redox reactions, degrading organic compounds such as methylene blue (MB).[11,12,15] Combining Au with TiO_2 enhances photocatalytic efficiency by broadening the light absorption spectrum to include visible light and improving charge separation, thereby reducing electron–hole recombination and enhancing overall photocatalytic performance.[12] Using recovered Au and TiO_2 from metallurgical waste offers significant cost savings and environmental benefits compared to commercially synthesized nanoparticles, which often require expensive precursors and energy-intensive processes. Reforming these materials reduces production costs, which aligns well with sustainable practices, minimizing the demand for extraction of virgin resources while reducing waste volume.

In this study, we explore the potential of completely regenerated and reformed Au–TiO_2 hybrid quantum dots (R-Au–TiO_2 QDs) as a sustainable and efficient photocatalyst for environmental applications, offering a novel approach to regenerating valuable materials while addressing the environmental challenges posed by the waste. In their reformed state, we have demonstrated the structural and surface integrity of R-Au–TiO_2. The photocatalytic performance of R-Au–TiO_2 QDs was evaluated through the degradation of MB in flexible, wearable composite films on aluminum foil substrates under various light conditions, including a solar simulator, UV light at 254 nm, and natural sunlight. The results reveal that R-Au–TiO_2 QDs exhibit superior photocatalytic activity compared to commercial TiO_2, particularly under UV light, with a degradation rate of 82.5%. This enhanced performance, attributed to the plasmonic effect of Au nanoparticles, suggests that R-Au–TiO_2 QDs are highly effective for applications such as water purification and environmental monitoring. By utilizing reformed materials, this study advances photocatalysis and supports the development of a circular economy, promoting sustainability and reducing the environmental impact of metallurgical waste.

2. Results and discussion

Fig. 1 presents a comprehensive comparison between R-Au–TiO_2 QDs and C-TiO_2 through various characterization techniques. Fig. 1a shows the X-ray diffraction (XRD) pattern for R-Au–TiO_2 QDs. The R-Au–TiO_2 QDs exhibit characteristic peaks corresponding to the anatase phase, with a high phase purity of 99.8%, indicating a successful recovery from the industrial waste. The XRD peaks for R-Au–TiO_2 QDs were matched against the Inorganic Crystal Structure Database (ICSD) reference pattern 154607, confirming a tetragonal crystal system with a space group of $I4_1/amd$. The presence of Au nanoparticles is confirmed by a distinct peak around $2\theta = 38°$, which matches the ICSD reference pattern 759732, indicating a cubic crystal system with a space group of $Fm\bar{3}m$, and a total Au content of 0.24%.

Rietveld refinement was performed to obtain detailed information on the crystal structure, including lattice parameters, phase composition, and particle size distribution. The calculated pattern from Rietveld refinement fits well with the observed data (Fig. 1a). The refinement parameters, R_{wp} (weighted profile R-factor) and R_{exp} (expected R-factor) are measures of the fit quality, where lower values indicate a better fit.[16,17] The refinement parameters for R-Au–TiO_2 QDs, $R_{wp} = 6.03$, $R_{exp} = 4.20$, and $G = 1.43$, indicate good fitting quality of the refinement process. The goodness-of-fit (G) value close to 1 implies an excellent match between observed and calculated patterns.[16,17] The difference plot in Fig. 1a shows the residuals between the observed and calculated patterns validating the refinement process. The crystallinity of R-Au–TiO_2 QDs was measured to be 100%, as detailed in the Experimental section. The high crystallinity of R-Au–TiO_2 QDs, evidenced by the sharp and well-defined XRD peaks, makes it a viable and sustainable alternative for sensing and photocatalytic applications.[15,18,19] The R-Au–TiO_2 QDs exhibit characteristic peaks corresponding to the anatase phase, with high crystalline phase purity as determined by Rietveld refinement of the XRD data, indicating successful recovery from the industrial waste. This phase composition is further supported by X-ray fluorescence (XRF) and inductively coupled plasma optical emission spectroscopy (ICP-OES) analyses (Table S1†), which confirm TiO_2 as the dominant component and Au nanoparticles as a minor functional additive.

Fourier transform infrared (FTIR) spectroscopy was conducted to analyze the chemical structure and identify the functional groups present in both R-Au–TiO_2 QDs and C-TiO_2 nanoparticles, helping to understand the surface chemistry and any potential modifications resulting from the reforming process. The FTIR spectra, shown in Fig. 1b, illustrate the transmittance (%) of both R-Au–TiO_2 QDs and C-TiO_2 across the wavenumber range of 650 to 4000 cm^{-1}. For R-Au–TiO_2 QDs, characteristic peaks are observed at 1126 cm^{-1}, 1631 cm^{-1}, and 2981 cm^{-1}. The peak at 1126 cm^{-1} is associated with Ti–O stretching vibrations that indicate the presence of titanium–oxygen bonds typical of the anatase phase.[20,21] The peak at 1631 cm^{-1} corresponds to the bending vibrations
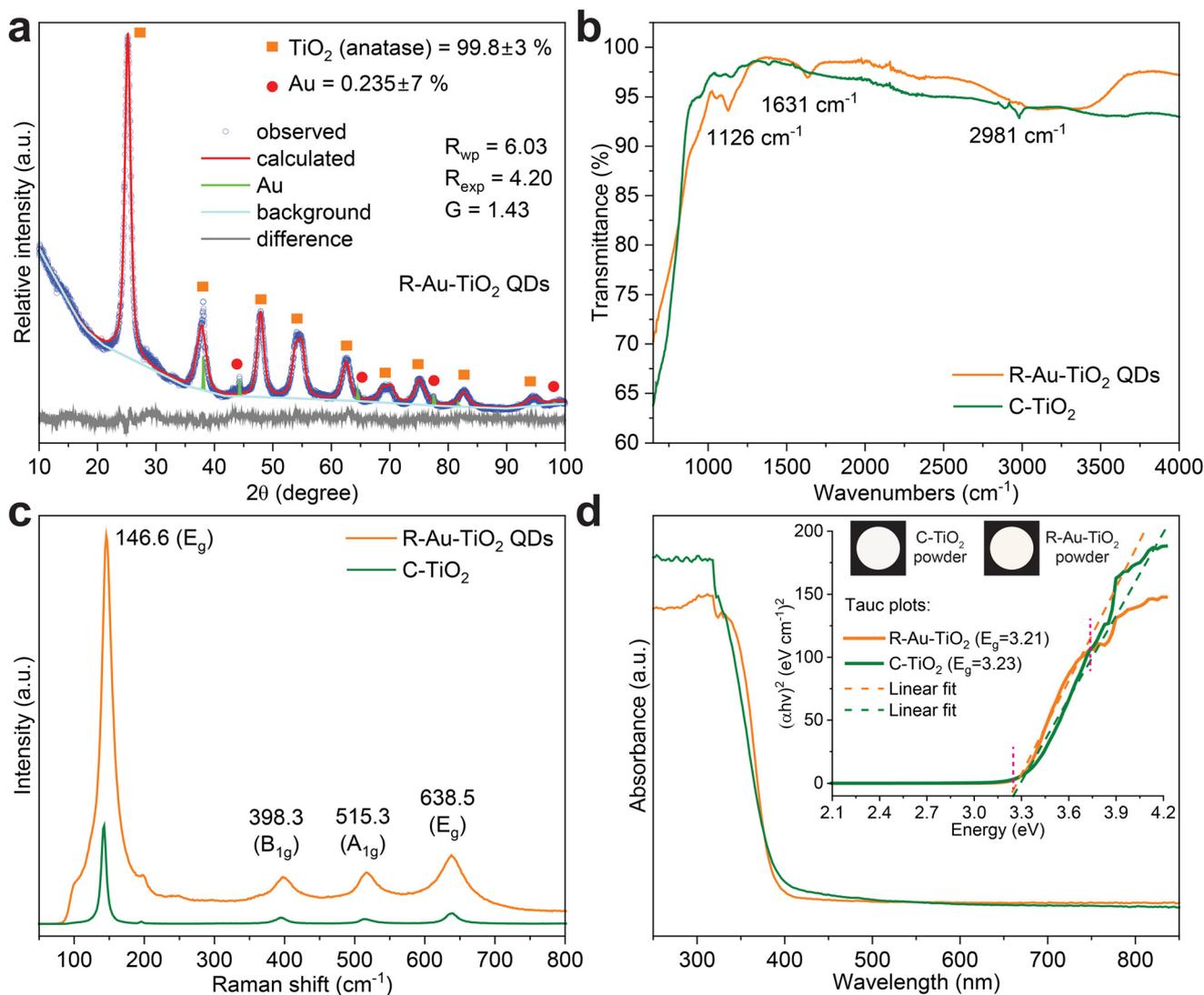
Fig. 1 (a) XRD patterns showing the anatase phase for R–Au–TiO$_2$ QDs, displaying a peak for Au nanoparticles. Rietveld refinement confirms high purity and crystallinity (b) FTIR spectra indicating Ti–O bonding and surface hydroxyl groups in R–Au–TiO$_2$ QDs, with higher moisture content compared to C-TiO$_2$ (c) Raman spectra revealing characteristic anatase phase peaks for both R–Au–TiO$_2$ QDs and C-TiO$_2$, indicating preserved crystalline structure post-reforming (d) UV-vis absorbance spectra showing strong UV absorption and slightly red-shifted absorption edge in R–Au–TiO$_2$ QDs due to Au nanoparticles. The inset includes Tauc plots indicating band gaps and powder colors calculated from UV-vis spectra.

of adsorbed water molecules, signifying the presence of surface hydroxyl groups, which are known to enhance photocatalytic activity by providing active sites for reaction.[22] The peak at 2981 cm^{-1} is attributed to C–H stretching vibrations, likely due to residual organic compounds from the reforming and synthesis process.[22] The observed blue shift of the Ti–O stretching peak to 1126 cm^{-1} in R–Au–TiO$_2$ QDs, compared to C-TiO$_2$, is attributed to quantum confinement effects associated with the sub-10 nm particle size, which can induce lattice strain and frequency shifts. Additionally, surface hydroxylation and residual organics, indicated by peaks at 1631 cm^{-1} and 2981 cm^{-1}, may influence the local bonding environment. Structural reorganization during the reforming process may further contribute to this shift.

The surface area of R–Au–TiO$_2$ QDs was measured to be 131.4 m^2 g^{-1} using Brunauer–Emmett–Teller (BET) analysis. A higher surface area typically enhances photocatalytic efficiency by providing more active sites for reactions and improving the interaction between the catalyst and analytes.[22] The variations in peak positions and intensities in FTIR spectra between R–Au–TiO$_2$ QDs and C-TiO$_2$ nanoparticles can be attributed to the presence of these residual organic compounds or slight structural modifications during the reforming process of R–Au–TiO$_2$ QDs. The increased moisture content in R–Au–TiO$_2$ QDs, as indicated by the more pronounced water adsorption peak, suggests that the reforming process may have introduced or retained more surface hydroxyl groups. These surface modifications could influence the photocatalytic and sensing pro-

perties of the material, potentially enhancing its performance.[23,24]

Raman spectroscopy was employed to investigate the vibrational properties and phase purity of both R-Au–TiO$_2$ QDs and C-TiO$_2$ nanoparticles. The Raman spectra in Fig. 1c reveal the vibrational modes of R-Au–TiO$_2$ QDs and C-TiO$_2$. For both samples, prominent peaks are observed at 146.6 cm^{-1} (E$_g$), 398.3 cm^{-1} (B$_{1g}$), 515.3 cm^{-1} (A$_{1g}$), and 638.5 cm^{-1} (E$_g$). These peaks are characteristic of the anatase phase of TiO$_2$.[25] The strong E$_g$ mode at 146.6 cm^{-1} is indicative of the symmetric stretching vibrations of the TiO$_6$ octahedra.[25] The peak at 398.3 cm^{-1} (B$_{1g}$) corresponds to the symmetric bending vibrations of the Ti–O bonds.[25,26] The 515.3 cm^{-1} (A$_{1g}$) peak represents the asymmetric bending vibrations of the Ti–O bonds.[26] The peak at 638.5 cm^{-1} (E$_g$) is due to the symmetric stretching vibrations of the Ti–O bonds. The similarity in peak positions and intensities between R-Au–TiO$_2$ QDs and C-TiO$_2$ indicates that the reforming process preserves the crystalline structure and vibrational properties of TiO$_2$. This suggests that the structural integrity of TiO$_2$ is maintained during the recovery process from industrial waste, making R-Au–TiO$_2$ QDs a suitable material for applications requiring high phase purity and crystallinity.[27,28]

Next, ultraviolet–visible (UV-vis) spectroscopy was performed to evaluate the optical properties and band gap energies of both R-Au–TiO$_2$ QDs and C-TiO$_2$ nanoparticles. These measurements are crucial for understanding the light absorption capabilities and potential applications of R-Au–TiO$_2$ QDs in UV detection and photocatalysis.[27] Fig. 1d displays the UV-vis absorbance spectra of R-Au–TiO$_2$ QDs and C-TiO$_2$. Both samples exhibit strong absorption in the UV region, with absorption edges around 390 nm.[27] The inset Tauc plots, as detailed in the Experimental section, indicate direct band gaps of 3.21 eV for R-Au–TiO$_2$ QDs and 3.23 eV for C-TiO$_2$.[29] The slight red shift in the absorption edge of R-Au–TiO$_2$ QDs can be attributed to the presence of Au nanoparticles, which enhance light absorption through LSPR effects.[30,31] Additionally, the inset of Fig. 1d shows the actual colors of both R-Au–TiO$_2$ QDs and C-TiO$_2$ powders, as calculated from the UV-vis spectra. The slight color difference can be attributed to the particle size difference, a relatively higher moisture content, and presence of Au nanoparticles in R-Au–TiO$_2$ QDs, which influence the optical properties.

Scanning electron microscopy (SEM) was performed to investigate the surface morphology and particle size distribution of both R-Au–TiO$_2$ QDs and C-TiO$_2$ nanoparticles. This analysis is crucial for confirming the physical structure and consistency of the synthesized nanoparticles, which are key factors for their application in various technologies. Fig. 2a presents the SEM micrograph of R-Au–TiO$_2$ QDs, while Fig. 2b shows the SEM micrograph of C-TiO$_2$ nanoparticles. Both images reveal a similar agglomerated morphology, typical of TiO$_2$ nanoparticles.[27] The average particle size in both R-Au–TiO$_2$ QDs and C-TiO$_2$ nanoparticles was found to be smaller than 20 nm, with the Au–TiO$_2$ QDs being smaller than 10 nm (Fig. S2†). The high-resolution SEM images illustrate that the R-Au–TiO$_2$ QDs maintain a uniform and consistent structure, comparable to that of the commercial counterpart (Fig. S1†).

High-resolution transmission electron microscopy (HR-TEM) analysis was conducted to obtain detailed information about the particle size, shape, degree of agglomeration, and crystallinity of the R-Au–TiO$_2$ QDs. Fig. 2c presents the HR-TEM image of R-Au–TiO$_2$ QDs, revealing well-dispersed particles with a uniform size distribution, which is crucial for consistent performance in various applications.[32] The average particle size is less than 10 nm, which is the threshold for QD size. Despite some degree of agglomeration, the HR-TEM image shows that the QDs retain their individual identities while remaining physically clustered (Fig. S2†). This is important for maintaining the high surface area and reactivity of the particles.[33] Furthermore, the high-resolution image confirms the high crystallinity of the R-Au–TiO$_2$ QDs (Fig. 2c). The lattice fringes observed in the HR-TEM image indicate well-defined crystal planes, demonstrating that the reforming and synthesis process preserves the crystalline structure of the R-Au–TiO$_2$ QDs (Fig. 2c and Fig. S2†). This high crystallinity is essential for applications that require efficient electron transport and optimal optical properties.[34]

Selected area electron diffraction (SAED) analysis was performed to investigate the crystalline structure and phase purity of the R-Au–TiO$_2$ QDs. Fig. 2d shows the SAED pattern of R-Au–TiO$_2$ QDs, displaying distinct planes that correspond to the anatase phase of TiO$_2$ with indices (101), (004), (200), and (105).[35] These rings indicate the presence of well-defined crystal planes, further confirming the high crystallinity of the R-Au–TiO$_2$ QDs. Additionally, the presence of Au nanoparticles is indicated by the (111) diffraction plane, validating the incorporation of Au within the TiO$_2$ matrix.[36] The clear and sharp diffraction spots in the SAED pattern confirm the high crystallinity and phase purity of the R-Au–TiO$_2$ QDs.

Energy-dispersive X-ray spectroscopy (EDX) and scanning transmission electron microscopy (STEM) analyses were performed to investigate the elemental composition and spatial distribution of elements within the R-Au–TiO$_2$ QDs. Fig. 2e presents the EDX elemental maps for Ti, O, and Au in R-Au–TiO$_2$ QDs. The uniform distribution of Ti and O elements indicates the homogeneous composition of the TiO$_2$ QDs. The presence of Au nanoparticles is confirmed by the EDX map, which shows discrete spots corresponding to Au nanoparticles. The EDX elemental maps demonstrate that the Ti and O elements are evenly distributed throughout the R-Au–TiO$_2$ QDs. The discrete spots of Au observed in the EDX map confirm that Au nanoparticles are integrated within the TiO$_2$ matrix.

Furthermore, energy-dispersive spectroscopy (EDS) analysis was conducted to quantify the elemental composition of both R-Au–TiO$_2$ QDs and C-TiO$_2$, as shown in Fig. 2f. The prominent peaks for Ti and O in both samples confirm the TiO$_2$ composition. The additional peaks for Au in the R-Au–TiO$_2$ QDs spectrum verify the presence of Au nanoparticles. The presence of carbon (C) and sulfur (S) peaks is due to the carbon coating used for SEM analysis and residual sulfur from the recovery process, respectively.[37,38]

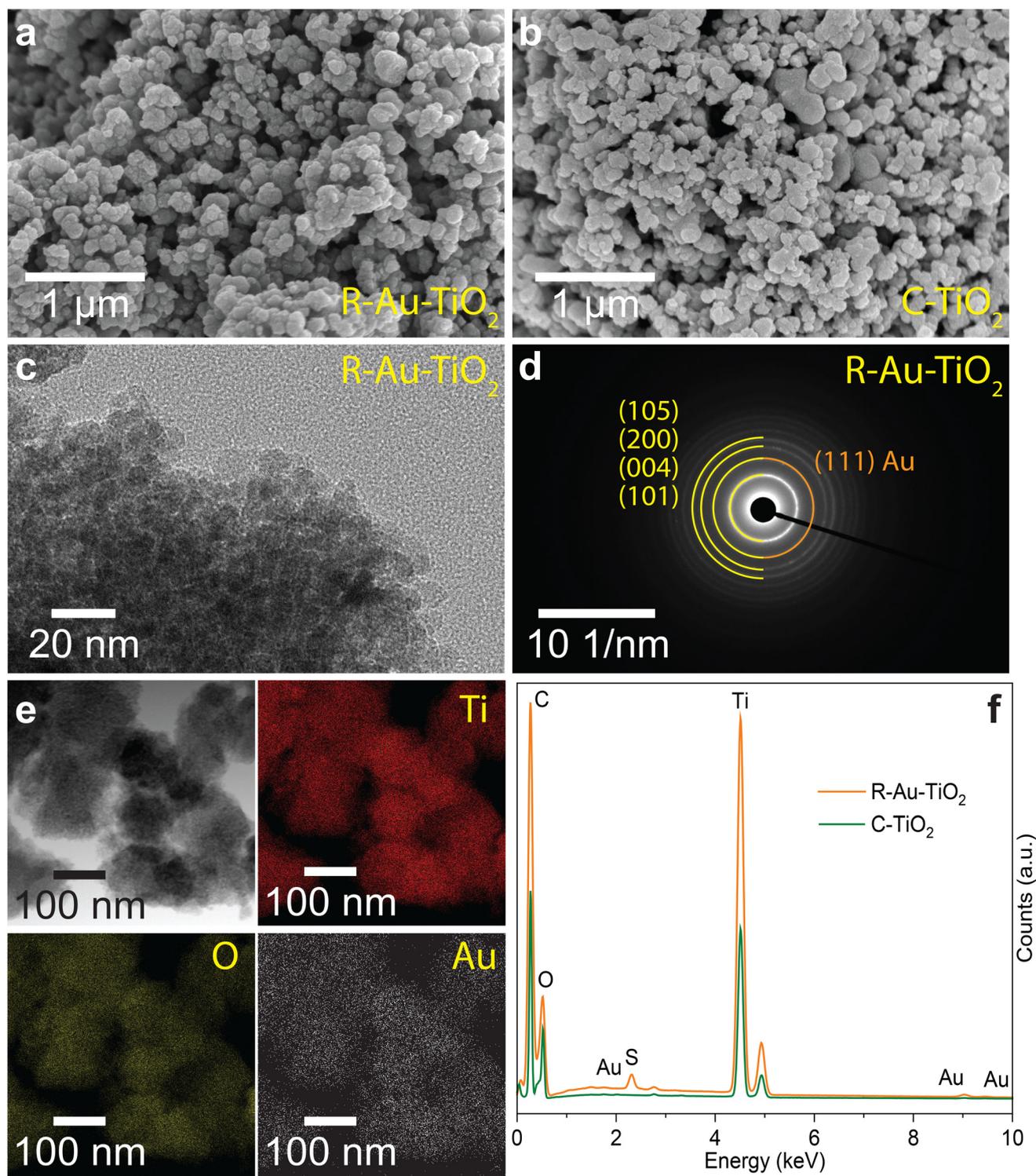**Fig. 2** (a) SEM image of R-Au–TiO$_2$ QDs, showing a similar agglomerated morphology to commercial TiO$_2$ in panel (b). (b) SEM image of C-TiO$_2$ nanoparticles (c) HR-TEM image of R-Au–TiO$_2$ QDs, revealing well-dispersed QDs with uniform size distribution and high crystallinity, confirmed by lattice fringes. (d) SAED pattern of R-Au–TiO$_2$ QDs, displaying distinct diffraction rings corresponding to the anatase phase of TiO$_2$ and the presence of Au nanoparticles (e) EDS elemental maps for Ti, O, and Au in R-Au–TiO$_2$ QDs, indicating a homogeneous composition of TiO$_2$ and discrete spots of Au nanoparticles (f) EDS spectra of both R-Au–TiO$_2$ QDs and C-TiO$_2$, showing prominent peaks for Ti and O, and additional peaks for Au in R-Au–TiO$_2$ QDs, highlighting the presence of regenerated Au nanoparticles.

Overall, the characterizations presented in Fig. 1 and 2 confirm that R-Au–TiO$_2$ QDs recovered from waste, exhibit structural, vibrational, and optical properties closely matching those of C-TiO$_2$ nanoparticles. This demonstrates the effectiveness of the reforming process and the potential of R-Au–TiO$_2$ QDs as a cost-effective and viable alternative to commercial TiO$_2$ for applications in UV detection, organic degradation, and other technologies.

Next, we investigated the light detection and degradation capabilities of MB in flexible polymer films (200 μm thick) composed of R-Au–TiO$_2$ QDs and C-TiO$_2$ nanoparticles on aluminum foil substrates. Fig. 3 presents a comprehensive analysis of the reflectance spectra and degradation rates for MB under different light conditions, specifically a solar simulator and UV light at 254 nm. The transmittance spectra are crucial for analyzing the degradation process, as they provide direct information on how much light passes through the film at different wavelengths. In this context, the region around 600–700 nm is of particular interest because it corresponds to the absorption peak of MB. A decrease in absorption at this wavelength, indicated by an increase in transmittance, signifies MB degradation, as less dye remains to absorb the light.[39]

The initial reflectance values before any light exposure for R-Au–TiO$_2$ QDs and C-TiO$_2$, with MB concentrations of 30 μL in both films, were 19% and 17% at 664 nm, respectively (Fig. 3a and b). Both spectra show a baseline reflectance level with a significant decrease around 600–700 nm due to MB absorption. Upon exposure to the solar simulator and UV light for 1 hour, the reflectance values for R-Au–TiO$_2$ QDs film increased to 34.3% and 33.8% at 664 nm, respectively, indicating MB degradation leading to less absorption and higher reflectance.[39] Similarly, the reflectance for C-TiO$_2$ increased to 29% under the solar simulator and 24% under UV light after 1 hour of exposure, which indicates MB degradation and film discoloration.

Fig. 3c illustrates the rate of MB degradation for R-Au–TiO$_2$ QDs and C-TiO$_2$ films under different light exposures. The degradation rates were determined by measuring the change in reflectance at the characteristic wavelength of MB (664 nm) before and after 1 hour of light exposure. R-Au–TiO$_2$ QDs exhibited degradation rates of 35% (0.59% min^{-1}) under the solar simulator and 34% (0.57% min^{-1}) under UV light. In comparison, C-TiO$_2$ showed degradation rates of 31% (0.51% min^{-1}) and 19% (0.32% min^{-1}) under the same conditions. These results confirm that R-Au–TiO$_2$ QDs outperform C-TiO$_2$ under both light conditions, with a more pronounced advantage under UV light, highlighting its superior photocatalytic performance.

Fig. 3d presents the visual discoloration of the flexible sensors composed of R-Au–TiO$_2$ QDs and C-TiO$_2$ before and after light exposure. Sensors with both 30 μL and 120 μL MB concentrations were prepared, and the color changes were measured using UV-vis spectroscopy to visually indicate the degree of MB degradation. The rate constants, k, for MB degradation under these light conditions were calculated using the first-order kinetics formula, $k = \dfrac{-\ln\left(\dfrac{A}{A_0}\right)}{t}$, where A and A_0 are the absorbance values after and before light exposure, respectively, and t is the exposure time (60 minutes).[39,40]

For the sensors with 30 μL MB concentration, the rate constants for R-Au–TiO$_2$ QDs under the solar simulator and UV light were approximately 0.0097 min^{-1} and 0.0095 min^{-1}, respectively. For C-TiO$_2$, the rate constants were approximately 0.0065 min^{-1} and 0.0036 min^{-1} under the same conditions. These findings confirm that R-Au–TiO$_2$ QDs sensors are more effective than C-TiO$_2$ sensors under both light conditions.

For the sensors with 120 μL MB concentration, the rate constants for R-Au–TiO$_2$ QDs were 0.0035 min^{-1} under the solar simulator and 0.0022 min^{-1} under the UV light (Fig. 3e). In contrast, C-TiO$_2$ exhibited rate constants of 0.0041 min^{-1} and 0.0014 min^{-1} under the same conditions (Fig. 3f). Notably, R-Au–TiO$_2$ QDs sensors exhibit a higher rate constant under UV light, suggesting its better performance under this specific condition. However, 1 hour of exposure may not fully capture MB degradation and film discoloration at higher MB concentrations. Therefore, sensors were exposed to light for extended periods to achieve complete MB degradation, as detailed in Fig. 4.

Fig. 4a and b present the transmittance spectra of R-Au–TiO$_2$ QDs and C-TiO$_2$ films, respectively, before and after 11 hours of exposure to solar simulator and UV light at 254 nm. The extended exposure time was chosen to thoroughly investigate the long-term effects of sustained light exposure on MB degradation, simulating real-world applications where the wearable sensor is exposed to light for extended periods.

For R-Au–TiO$_2$ QDs, the transmittance spectra in Fig. 4a show significant changes after 11 hours of light exposure. Initially, the film exhibits a deep absorption band around 600–700 nm. After 11 hours under the solar simulator, transmittance in this region increases markedly, indicating a substantial portion of the MB has been degraded. The degradation rate under the solar simulator was calculated to be 68%, with a degradation rate per minute of 1.14% min^{-1}, and a rate constant of 0.0192 min^{-1}. When exposed to UV light for 11 hours, R-Au–TiO$_2$ QDs show an even greater increase in transmittance, with a degradation rate of 82.5%, a degradation rate per minute of 1.38% min^{-1}, and a rate constant of 0.0291 min^{-1}. The more pronounced increase in transmittance under UV light is attributed to the higher energy of UV photons, which induce more efficient photocatalytic reactions.

In comparison, the transmittance spectra for C-TiO$_2$ in Fig. 4b also show significant increases after 11 hours of light exposure. Initially, the spectrum displays a deep absorption band around 600–700 nm. After exposure to the solar simulator, transmittance in this region increases, corresponding to a degradation rate of 69%, a degradation rate per minute of 1.16% min^{-1}, and a rate constant of 0.0199 min^{-1}. These values suggest that C-TiO$_2$ performs slightly better than R-Au–TiO$_2$ QDs under the solar simulator. Under UV light, however, C-TiO$_2$ exhibits a lower degradation rate compared to R-Au–
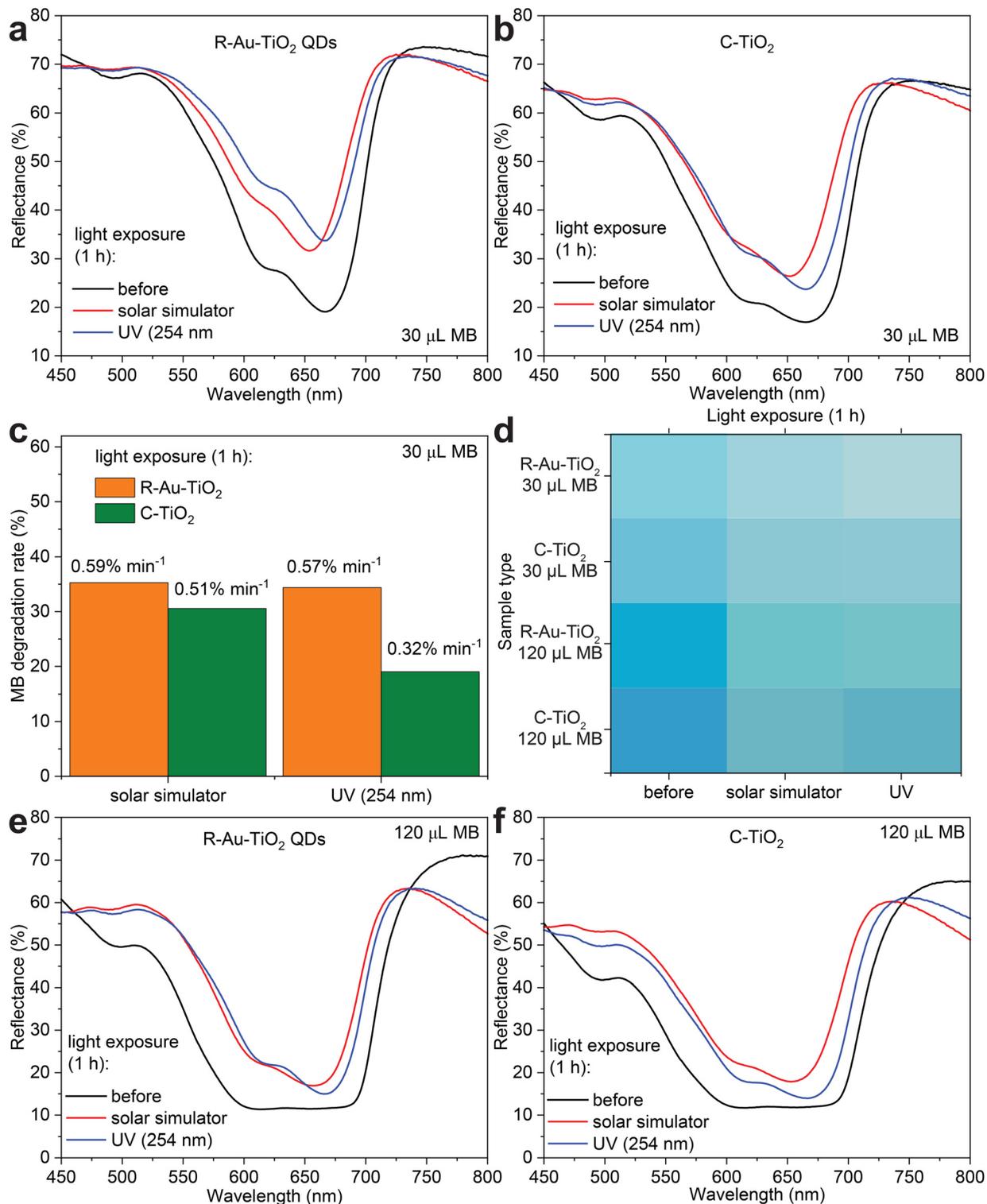
Fig. 3 Reflectance spectra of (a) R-Au–TiO$_2$ QDs and (b) C-TiO$_2$ films with 30 μL MB before and after 1 hour of exposure to a solar simulator and UV (254 nm) (c) comparison of MB degradation rates for R-Au–TiO$_2$ QDs and C-TiO$_2$ (30 μL MB) after 1 hour exposure to solar simulator and UV (254 nm) (d) actual colors of flexible sensors composed of R-Au–TiO$_2$ QDs and C-TiO$_2$ before and after light exposure. Reflectance spectra of (e) R-Au–TiO$_2$ QDs and (f) C-TiO$_2$ films with 120 μL MB before and after 1 hour of exposure to a solar simulator and UV (254 nm).
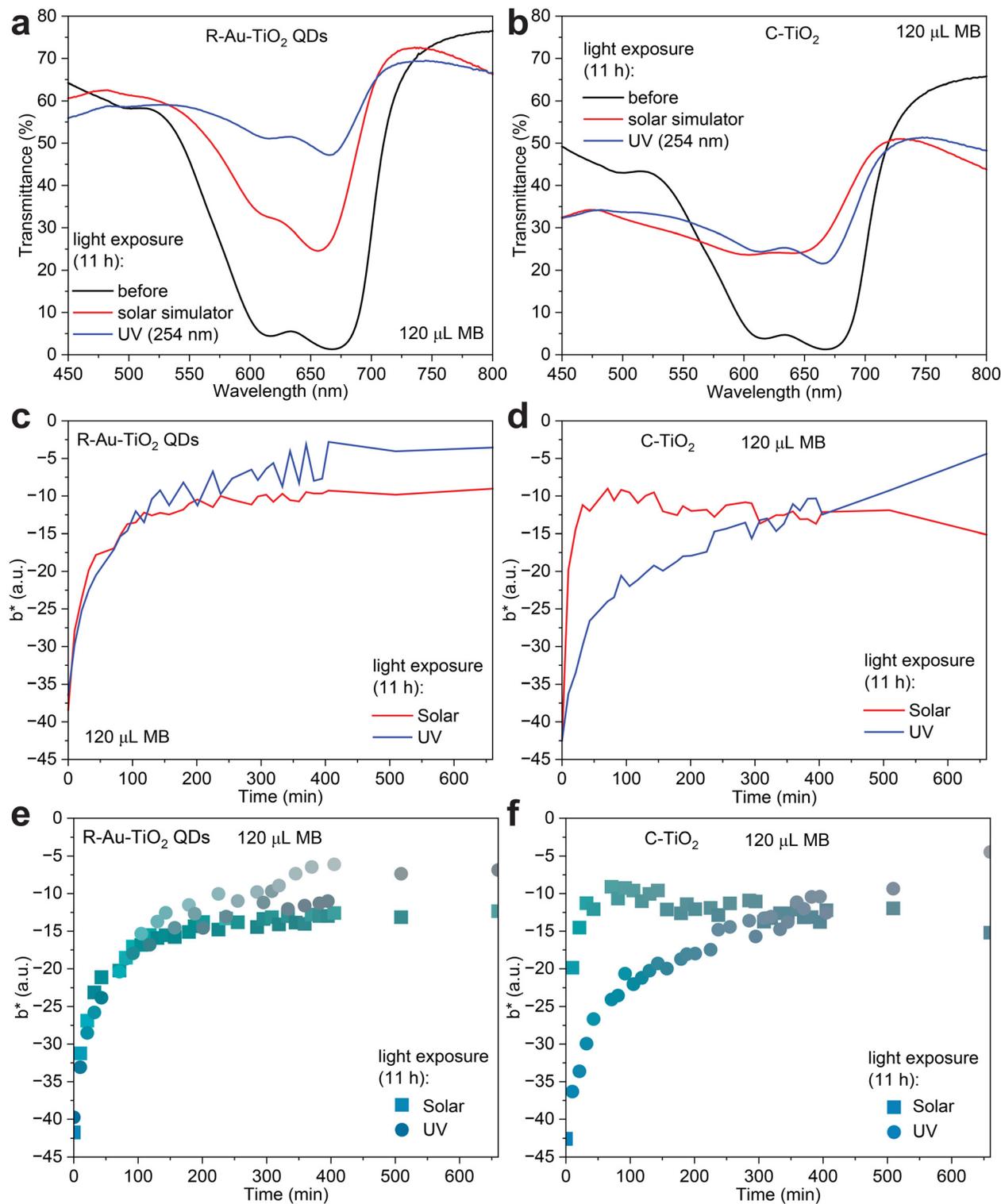
Fig. 4 (a) Transmittance spectra of R–Au–TiO$_2$ QDs films before and after 11 hours of exposure to solar simulator and UV light at 254 nm, showing significant MB degradation (b) transmittance spectra of C-TiO$_2$ films under the same conditions, indicating effective but slightly less pronounced MB degradation compared to R–Au–TiO$_2$ QDs (c) b^* component of the CIELAB color system for R–Au–TiO$_2$ QDs films, measured over time during 11 hours of light exposure, showing a significant increase under UV light (d) b^* component for C-TiO$_2$ films, showing a more gradual increase, indicating less effective MB degradation (e) actual colors of R–Au–TiO$_2$ QDs films presented in sRGB values over time, visually demonstrating the color change due to MB degradation (f) actual colors of C-TiO$_2$ films in sRGB values, showing a similar but less intense color change.

TiO_2 QDs, with a rate of 64.5%, a degradation rate per minute of 1.07% min^{-1}, and a rate constant of 0.0173 min^{-1}. This indicates that while C-TiO_2 is still effective at degrading MB under UV light, its performance is not as robust as that of R-Au–TiO_2 QDs, especially under UV light.

The differences in transmittance spectra between R-Au–TiO_2 QDs and C-TiO_2 after 11 hours of exposure highlight the enhanced photocatalytic efficiency of R-Au–TiO_2 QDs under UV light, likely due to the presence of Au nanoparticles that enhance the light absorption through LSPR effects.

Fig. 4c and d present the b^* component of the CIELAB (Commission Internationale de l'Éclairage $L^*a^*b^*$) color system for the R-Au–TiO_2 QDs and C-TiO_2 sensors, respectively, as a function of time during 11 hours of exposure to the solar simulator and UV light. The CIELAB color system, specified by the International Commission on Illumination (CIE), models human vision and represents colors in a perceptually uniform way.[32,41] The system consists of three axes: L^*, which represents lightness; a^*, which represents the color spectrum from green to red; and b^*, which represents the color spectrum from blue to yellow.[42] The b^* component is particularly relevant in this study as it reflects the degree of yellowing or bluing of the sample, directly correlating with MB degradation in films.[39] As MB degrades, it loses its characteristic blue color, leading to changes in the b^* value. These color measurements were obtained directly from the sensors using a Nix Mini Color Sensor, a handheld device that provides accurate and consistent readings of the color in CIELAB and standard RGB (sRGB) coordinates. This approach allows for a non-destructive and precise quantitative method of monitoring the progress of MB degradation over time.

Fig. 4c shows the b^* values for R-Au–TiO_2 QDs over the 11 hour light exposure period. Initially, the b^* value is relatively low, reflecting the presence of MB, which imparts a blue tint to the film. As exposure time increases, the b^* value rises, indicating a shift toward the yellow part of the spectrum, corresponding to MB degradation. Under the solar simulator, the b^* value increases steadily, indicating continuous MB degradation. However, under UV light, the increase in b^* is more pronounced, suggesting that UV light is more effective in degrading MB in the R-Au–TiO_2 QDs film. This result aligns with the transmittance data, where UV exposure led to a higher degradation rate.

Fig. 4d shows the b^* values for C-TiO_2 under the same conditions. The b^* value for C-TiO_2 also increases over time as MB degrades, but the rate of increase under both the solar simulator and UV light is slightly lower than that observed for R-Au–TiO_2 QDs, which is consistent with the slightly lower degradation rates seen in the transmittance spectra (Fig. 4b). The solar simulator causes a moderate increase in b^* over time, while the UV light induces a more gradual rise, indicating that C-TiO_2 is less effective in degrading MB compared to R-Au–TiO_2 QDs under UV conditions.

The b^* plots in Fig. 4c and d are directly related to MB degradation, providing a quantitative measure of the color change associated with the loss of MB in the films. The greater change in b^* under UV light for R-Au–TiO_2 QDs underscores its superior photocatalytic capabilities, especially in conditions where high-energy light sources are used.

In addition to analyzing the b^* component, we also examined the a^* component of the CIELAB color system, as shown in the ESI (Fig. S3†). The a^* component, which represents the green to red color spectrum, offers further insights into the color changes occurring as MB degrades. Initially, both sensors exhibit smaller a^* values, indicating a greenish tint due to the presence of MB. As exposure time increases, the a^* values rise, signifying a shift toward the red spectrum, correlating with MB degradation. For R-Au–TiO_2 QDs, the a^* increase is more pronounced under UV light, aligning with the higher degradation rates observed. C-TiO_2 also shows an increase in a^*, but to a lesser extent, particularly under UV light, indicating a lower degree of MB degradation. These a^* measurements complement the b^* analysis presented in Fig. 4c and d, collectively highlighting the enhanced photocatalytic performance of R-Au–TiO_2 QDs, especially under UV conditions.

Fig. 4e and f present the b^* component of the CIELAB color system, similar to Fig. 4c and d, but with the actual colors captured by the color sensor displayed in sRGB values. These plots visually represent the color changes associated with MB degradation in R-Au–TiO_2 QDs and C-TiO_2 films during 11 hours of exposure to the solar simulator and UV light. In Fig. 4e, the R-Au–TiO_2 QDs sensor shows a noticeable shift from a blue–green hue to a more yellowish color over time, reflecting the increase in the b^* value as MB degrades. The color change is more pronounced under UV light, which aligns with the higher degradation rate observed in previous analyses. Fig. 4f shows a similar trend for the C-TiO_2 sensor, with the colors shifting toward yellow as MB degrades. However, the color change is less intense compared to R-Au–TiO_2 QDs, particularly under UV light, indicating a slower degradation process. Fig. S4† also visually presents the color changes over 11 hours of light exposure, directly showing the transition from blue green to yellow as MB degrades in R-Au–TiO_2 QDs and C-TiO_2 films. These visual representations in sRGB format effectively demonstrate the extent of MB degradation, complementing the quantitative b^* data and further confirming the superior photocatalytic performance of R-Au–TiO_2 QDs, especially under UV light exposure.

In addition to the solar simulator and UV light at 254 nm, a range of experiments using natural sunlight were also conducted to evaluate the photocatalytic performance of R-Au–TiO_2 QDs and C-TiO_2 films. As shown in Fig. S5,† the reflectance spectra for both R-Au–TiO_2 QDs and C-TiO_2 films were measured before and after 1 hour of exposure to natural sunlight. The results indicate that R-Au–TiO_2 QDs exhibit a more significant decrease in reflectance at 600–700 nm, corresponding to a greater degree of MB degradation, compared to C-TiO_2. These findings suggest that R-Au–TiO_2 QDs are not only effective under controlled light conditions but also demonstrate robust performance in real-world sunlight exposure, positioning them as promising candidates for practical environmental remediation applications. Table S2† pro-

vides a comparative overview of different TiO$_2$ preparation methods, sources, substrates, and photocatalytic performance, highlighting the comparable and even superior performance of reformed and regenerated Au–TiO$_2$ QDs in this study.

The photocatalytic properties of TiO$_2$ and the mechanisms underlying the degradation of organic dyes such as MB are well-documented in the literature.[23,27,38,43] However, this study aims to demonstrate that reformed and regenerated materials from waste resources, specifically Au–TiO$_2$ QDs, can exhibit properties comparable to or even superior to their commercial counterparts. Fig. 5 illustrates the proposed mechanism of MB degradation and sensing in both C-TiO$_2$ and R-Au–TiO$_2$ QDs. The primary mechanism involves the excitation of TiO$_2$ nanoparticles under light irradiation, generating electron–hole pairs that participate in redox reactions to degrade MB molecules (Fig. 5a and b).[44] When TiO$_2$ absorbs photons with energy equal to or greater than its bandgap (3.2 eV), electrons in the valence band are excited to the conduction band, leaving behind holes in the valence band, represented by the equation: $TiO_2 + h\nu \rightarrow TiO_2 (e^- + h^+)$. The excited electrons and holes then migrate to the surface of the TiO$_2$ nanoparticles, where they participate in oxidation and reduction reactions.[29]

For MB degradation under UV light at 254 nm, UV light excites the TiO$_2$, creating electron–hole pairs. The electrons reduce adsorbed moisture or oxygen to superoxide radicals (O_2^-), while the holes oxidize water or hydroxide ions to hydroxyl radicals ($OH^\bullet$), as shown in the reactions: $e^- + O_2 \rightarrow O_2^-$ and $h^+ + H_2O \rightarrow {}^\bullet OH + H^+$.[29] These radicals react with MB molecules, leading to their degradation and mineralization: ${}^\bullet OH + MB \rightarrow$ degraded products and ${}^\bullet O_2^- + MB \rightarrow$ degraded products. Under the solar simulator and natural sunlight, similar reactions occur. However, R-Au–TiO$_2$ QDs sensor demonstrates superior performance under UV light, with a higher degradation rate compared to the solar simulator and sunlight, indicating that the high energy of UV photons significantly enhances the photocatalytic efficiency.[43,44]

The enhanced photocatalytic activity of R-Au–TiO$_2$ QDs is attributed to the LSPR effect of Au nanoparticles. The red-shift in the UV-vis absorption edge (Fig. 1d), along with Au incorporation confirmed by XRD, SAED, and EDS, supports this

mechanism. LSPR-induced hot electrons may be injected into the conduction band of TiO$_2$, facilitating charge separation and reducing recombination. Similar effects have been reported in Au–TiO$_2$ systems with sub-1 wt% Au loadings.[11,12,35] This process is illustrated in Fig. 5b and can be described as: $Au + h\nu \rightarrow Au \rightarrow Au + e^-$, where the hot electron is injected into the conduction band (CB) of TiO$_2$.

Additionally, Au nanoparticles may act as electron sinks, reducing the recombination rate of electron–hole pairs and prolonging carrier lifetimes.[43] While the enhancement is most pronounced under UV light, the R-Au–TiO$_2$ QDs also show improved photocatalytic performance under solar simulator and natural sunlight, suggesting that the plasmonic effect contributes across multiple light conditions. While the R-Au–TiO$_2$ QDs investigated in this study contained 0.24 wt% Au as recovered from waste, future work will focus on systematically tuning the Au:TiO$_2$ ratio to optimize photocatalytic performance and material cost. Literature suggests that excessive Au loading may lead to performance saturation or decline due to plasmonic damping and surface shielding effects. Systematic composition optimization is therefore warranted to fully realize the application potential of this material.

The practical application of these flexible and wearable films includes their use as sensors in environmental monitoring or water purification systems, where the degradation of organic pollutants such as MB is critical. The use of the solar simulator and UV light at 254 nm in this study was designed to replicate conditions these sensors would encounter in real-world applications, ensuring that they perform effectively across a range of light environments.

In addition to their functional performance, the R-Au–TiO$_2$ QDs offer sustainability advantages by utilizing industrial waste as the sole feedstock through a low-cost, low-temperature process. A performance comparison with reported TiO$_2$-based systems is provided in Table S2 (ESI†), demonstrating their competitive activity alongside circular economy benefits.

3. Conclusion

This study demonstrated that R-Au–TiO$_2$ QDs, regenerated from industrial waste, exhibit superior photocatalytic performance compared to commercial TiO$_2$, particularly under UV light. The R-Au–TiO$_2$ QDs achieved an MB degradation rate of 82.5% and a rate constant of 0.0291 min^{-1}, outperforming C-TiO$_2$ (64.5%, 0.0173 min^{-1}) under 254 nm UV exposure. The b^* component from the CIELAB color system showed a more pronounced shift in R-Au–TiO$_2$ films, further confirming enhanced activity.

The improved performance is attributed to the sub-10 nm particle size and the presence of Au nanoparticles, which enhance light absorption through localized surface plasmon resonance (LSPR) and improve charge separation by acting as electron sinks. These structural features contribute to reduced electron–hole recombination and prolonged charge carrier lifetimes.
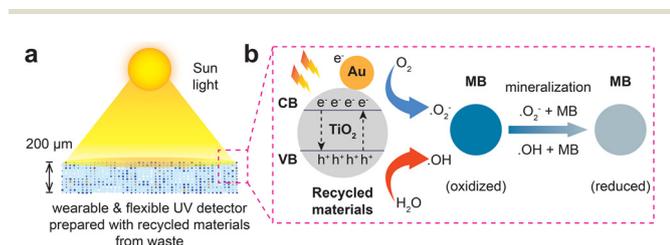

Fig. 5 (a) Schematic illustration of the MB degradation and sensing mechanism for C-TiO$_2$ and R-Au–TiO$_2$ QDs containing Au nanoparticles (b) TiO$_2$ nanoparticles absorb light to generate electron–hole pairs, with Au nanoparticles in R-Au–TiO$_2$ QDs enhancing photocatalytic activity through the plasmonic effect and improved charge separation, leading to more efficient MB degradation under solar simulator and UV light at 254 nm.

Unlike conventional TiO$_2$ synthesis methods that rely on synthetic precursors and high-temperature treatment (>450 °C), the regeneration process presented here uses a waste-derived Au–Ti alloy and operates at a moderate temperature of 300 °C. This reduces material costs, energy consumption, and waste generation. The process employs scalable industrial techniques such as leaching, precipitation, and low-temperature heat treatment, aligning with circular economy principles and supporting potential for industrial implementation.

These results highlight the potential of R-Au–TiO$_2$ QDs as a sustainable, low-cost alternative for photocatalytic applications in environmental monitoring and water purification. While MB was used as a model pollutant under controlled conditions, we acknowledge that real wastewater includes competing species and variable conditions. Future studies will explore the performance of R-Au–TiO$_2$ QDs in realistic environmental matrices to further assess their practical applicability.

4. Experimental

4.1. Reforming and regeneration process

R-Au–TiO$_2$ QDs were prepared using a leaching and precipitation method. A waste Au–Ti (50 wt%–50 wt%) alloy served as the starting material and was leached in aqua regia (HNO$_3$ + 3HCl). During the dissolution process, the solution temperature rose to 60–80 °C and was maintained until the alloy was fully dissolved. Titanium rapidly precipitated as TiO$_2$, as it has negligible solubility in aqueous media.[45,46]

During this spontaneous precipitation, Au species in the leachate, likely in the form of chloroauric acid (HAuCl$_4$), were partially incorporated onto or within the forming TiO$_2$ nanocrystals through physical attachment or entrapment. This process occurred without the use of chemical reducing agents or capping molecules and was driven by the concurrent presence of both species in solution.

The small particle size (<10 nm) of R-Au–TiO$_2$ QDs is attributed to the rapid nucleation and spontaneous precipitation of TiO$_2$ in the acidic leachate. In the absence of growth modifiers or high-temperature sintering, the particles form quickly and remain in the nanoscale range. Key parameters influencing particle size include the concentration of the leachate, the reaction temperature (maintained at 60–80 °C), and the rapid precipitation rate. The mild post-treatment at 300 °C prevents particle sintering, helping to preserve the small size of the resulting quantum dots.

The final Au content (0.24 wt%) in the regenerated R-Au–TiO$_2$ QDs was significantly lower than the initial 50 wt% in the alloy due to this selective precipitation behavior: titanium precipitated readily as TiO$_2$, while most gold remained dissolved. Unlike conventional Au recovery approaches, no chemical reduction step was applied in this process.

Some agglomeration was observed in the resulting particles (Fig. 2a), which is typical for sol–gel-like precipitation methods conducted without stabilizers. The aggregation likely occurs among TiO$_2$ particles rather than between Au and TiO$_2$. Although morphology control was not the focus of this work, future optimization may include surfactants, pH adjustment, or controlled precipitation to minimize particle agglomeration.

The particles were washed with deionised water and calcined at 300 °C to remove moisture and physically or chemically adsorbed species. The reforming process was repeated three times with separate batches of Au–Ti alloy waste. All batches produced R-Au–TiO$_2$ QDs with consistent Au content (0.24 wt%) and anatase TiO$_2$ purity exceeding 99.5%, confirming the reproducibility of the regeneration method.

4.2. Materials and methods

R-Au–TiO$_2$ QDs (99.8 wt% purity) with an average particle size of less than 10 nm, containing 0.24 wt% Au, were utilized to fabricate wearable and flexible UV sensors. Polyvinyl alcohol (PVA, with an average molecular weight (MW) of 85 000 g mol^{-1}) was procured from Merck, and methylene blue (MB, with an average molecular weight of 320 g mol^{-1}) was obtained from Acros Organics, Thermo Fisher Scientific. Both PVA and MB were used without further purification. Deionized water with a resistivity of 18 MΩ cm was used in all experiments. For comparative analysis, commercial TiO$_2$ (C-TiO$_2$) anatase (MW: 80 g mol^{-1}, ≥99 wt% purity), primary particle size 21 nm (TEM) was also purchased from Merck.

4.3. Sensor fabrication

The wearable and flexible film sensors were fabricated using a mixture of solutions comprising R-Au–TiO$_2$ QDs, PVA as a binder, and MB as an organic dye. The stock solutions were prepared as follows: 0.05 g of R-Au–TiO$_2$ QDs was added to 10 mL of deionized water and sonicated for 1 hour at 30 °C. Following this, 1 g of PVA was added to the solution, which was then stirred for 4 hours at 75 °C. A stock solution of MB was prepared by dissolving 45 mg of MB in 10 mL of deionized water. The resulting solution was used to create sensing films employing a commercial doctor blade technique on transparent glass and flexible aluminum substrates, achieving a uniform thickness of 200 μm. The doctor blade speed was set to 6 mm s^{-1} to ensure consistent thickness across 30 mm long aluminum substrates. The prepared films were dried at room temperature and stored in dark conditions. Small circular sensors, 10 mm in diameter, were then punched out using a manual punch press.

4.4. Light exposure experiments

The sensors were subjected to light exposure experiments using three different light sources: a solar simulator, UV light at 254 nm, and natural sunlight. For simulated sunlight exposure, a G2 V solar simulator with an intensity of 100 mW cm^{-2}, equivalent to one sun (AM1.5G), and a spectral range of 365 to 1100 nm was employed. UV exposure experiments utilized a low-power (8 watt) UV generator equipped with a UVP 3UV Lamp, provided by Analytik Jena US, to generate 254 nm UV light. The working distance was maintained at 7 cm from both the solar simulator and the UV generator. For natural

sunlight exposure, samples were directly exposed to sunlight through an office window from morning onwards. All samples were kept in dark conditions before and after each light exposure experiment. All light exposure experiments were repeated with independently prepared sensors under UV light, solar simulator, and natural sunlight. Consistent degradation responses across these three lighting environments confirm the reproducibility and reliability of the experimental results.

4.5. Characterization techniques

The R-Au–TiO$_2$ QDs, recovered from waste, were characterized using various techniques to investigate their size, morphology, purity, and surface area.

Phase identification and quantification were performed using a PANalytical Xpert Multipurpose X-ray Diffraction (XRD) system at room temperature with Cu Kα radiation (Kα1 = 1.54060 Å and Kα2 = 1.54443 Å). The XRD spectra were analysed and refined using a commercial PANalytical HighScore Plus software. The modified Scherrer equation is used to accurately estimate the crystal size of quantum dots from XRD peaks[47,48] and is given by, $\ln \beta = \ln\left(\dfrac{1}{\cos\theta}\right) + \ln\left(\dfrac{K\lambda}{D}\right)$, where β is full width at half-maximum, in radians, located at any 2θ position in the pattern, λ (nm) is the radiation of wavelength, K is the Scherrer constant or shape factor, and D is the particle size in nm.

Scanning electron microscopy (SEM) analysis was conducted using an FEI Nova NanoSEM 450 (FE-SEM), equipped with energy dispersive spectroscopy (EDS) provided by Bruker and Cambridge. Transmission electron microscopy (TEM) analysis was performed using an FE-TEM JEOL JEM-F200, operating at 200 kV, coupled with energy dispersive X-ray spectroscopy (EDX).

The surface area of the nanoparticles was determined using the Brunauer–Emmett–Teller (BET) method with a Micromeritics TriStar II 3020. Approximately 100 mg of the samples were analysed at 77.3 K in liquid nitrogen.

Fourier transform infrared (FTIR) analysis was performed using a PerkinElmer Spectrum 100 equipped with Spectrum V.10 software. The spectra were collected from 650 to 1800 cm^{-1} or 4000 cm^{-1} to qualitatively compare the R-Au–TiO$_2$ QDs and C-TiO$_2$ nanoparticles.

Raman data were acquired using a Renishaw inVia Raman microscope equipped with a He–Ne green laser (λ = 514 nm) and a diffraction grating of 1800 g mm^{-1}. The equipment was calibrated using the Si peak at approximately 520 cm^{-1}. Spectra were collected in the range of 50–800 cm^{-1} with a spot size of ~4 μm and analysed using Renishaw WiRE 4.4 software.

All UV-vis measurements, including absorbance, transmittance, and reflectance, were performed on the sensing films and R-Au–TiO$_2$ QDs powder using a LAMBDA 1050 UV/vis/NIR spectrophotometer (PerkinElmer) equipped with a snap-in 150 mm integrating sphere. Reflectance measurements were taken as percentages relative to a diffuse white standard (spectralon) in the wavelength range of 200 to 800 nm. The Tauc plot was used to compute the optical bandgap TiO$_2$ nanoparticles using Tauc and Davis-Mott relation from UV-vis absorption spectroscopy as described elsewhere.[49]

Data availability

The data supporting this article have been included as part of the ESI.† The ESI† includes: XRF and ICP-OES analysis results, SEM images comparing reformed Au–TiO$_2$ hybrid quantum dots and commercial TiO$_2$ nanoparticles at various magnifications, TEM images of R-Au–TiO$_2$ quantum dots at different scales, a^* component colorimetric analysis of R-Au–TiO$_2$ and C-TiO$_2$ during various light conditions, visual representation of color changes in R-Au–TiO$_2$ and C-TiO$_2$ films during different light exposure conditions, reflectance spectra before and after natural sunlight exposure for R-Au–TiO$_2$ and C-TiO$_2$ films with different MB concentrations, and a table overview of TiO$_2$-based materials for MB degradation under various light sources.

Conflicts of interest

There are no conflicts to declare.

Acknowledgements

References

1 D.-A. Iluțiu-Varvara and C. Aciu, *Sustainability*, 2022, **14**, 5488.

2 E. Matinde, G. S. Simate and S. Ndlovu, *J. South. Afr. Inst. Min. Metall.*, 2018, **118**, 825–844.

3 Z. Peng, D. Gregurek, C. Wenzl and J. F. White, *JOM*, 2016, **68**, 2313–2315.

4 I. M. Shatokhin, A. L. Kuz'min, L. A. Smirnov, L. I. Leont'ev, V. A. Bigeev and I. R. Manashev, *Metallurgist*, 2017, **61**, 523–528.

5 S. Ramachandra Rao, in *Metallurgical Slags, Dust and Fumes*, Elsevier, 2006, pp. 269–327.

6 M. A. Reuter, A. van Schaik, J. Gutzmer, N. Bartie and A. Abadías-Llamas, *Annu. Rev. Mater. Res.*, 2019, **49**, 253–274.

7 S. Singh, L. Sukla and S. Goyal, *Mater. Today: Proc.*, 2020, **30**, 332–339.

8 H. Yi, G. Xu, H. Cheng, J. Wang, Y. Wan and H. Chen, *Proc. Environ. Sci.*, 2012, **16**, 791–801.

9 B. Qiu, C. Yang, Q. Shao, Y. Liu and H. Chu, *Fuel*, 2022, **315**, 123218.

10 Z. Wu, M. Wang, Y. Bai, H. Song, J. Lv, X. Mo, X. Li and Z. Lin, *Chem. Eng. J.*, 2023, **464**, 142532.

11 L. I. Jinga, G. Popescu-Pelin, G. Socol, S. Mocanu, M. Tudose, D. C. Culita, A. Kuncser and P. Ionita, *Nanomaterials*, 2021, **11**, 1605.

12 C. Yogi, K. Kojima, N. Wada, H. Tokumoto, T. Takai, T. Mizoguchi and H. Tamiaki, *Thin Solid Films*, 2008, **516**, 5881–5884.

13 Z. U. Abideen, W. U. Arifeen and Y. M. N. D. Bandara, *Nanoscale*, 2024, **16**(19), 9259–9283.

14 Z. U. Abideen, W. U. Arifeen and A. Tricoli, *Nanoscale*, 2024, **16**(16), 7752–7785.

15 J. Wang, B. Liu and K. Nakata, *Chin. J. Catal.*, 2019, **40**, 403–412.

16 B. H. Toby, *Powder Diffr.*, 2006, **21**, 67–70.

17 L. B. McCusker, R. B. Von Dreele, D. E. Cox, D. Louër and P. Scardi, *J. Appl. Crystallogr.*, 1999, **32**, 36–50.

18 M. Inagaki, R. Nonaka, B. Tryba and A. W. Morawski, *Chemosphere*, 2006, **64**, 437–445.

19 G. Tian, H. Fu, L. Jing and C. Tian, *J. Hazard. Mater.*, 2009, **161**, 1122–1130.

20 M. Chi, X. Sun, G. Lozano-Blanco and B. J. Tatarchuk, *Appl. Surf. Sci.*, 2021, **570**, 151147.

21 M. Lal, P. Sharma and C. Ram, *Optik*, 2021, **241**, 166934.

22 P. A. Connor, K. D. Dobson and A. J. McQuillan, *Langmuir*, 1999, **15**, 2402–2408.

23 M. Humayun, F. Raziq, A. Khan and W. Luo, *Green Chem. Lett. Rev.*, 2018, **11**, 86–102.

24 D. Zhao, C. Chen, Y. Wang, H. Ji, W. Ma, L. Zang and J. Zhao, *J. Phys. Chem. C*, 2008, **112**, 5993–6001.

25 W. Su, J. Zhang, Z. Feng, T. Chen, P. Ying and C. Li, *J. Phys. Chem. C*, 2008, **112**, 7710–7716.

26 J. Prakash, S. Sun, H. C. Swart and R. K. Gupta, *Appl. Mater. Today*, 2018, **11**, 82–135.

27 X. Chen and S. S. Mao, *Chem. Rev.*, 2007, **107**, 2891–2959.

28 I. Ali, M. Suhail, Z. A. Alothman and A. Alwarthan, *RSC Adv.*, 2018, **8**, 30125–30147.

29 F. Azeez, E. Al-Hetlani, M. Arafa, Y. Abdelmonem, A. A. Nazeer, M. O. Amin and M. Madkour, *Sci. Rep.*, 2018, **8**, 7104.

30 Q. Li, J. Huang, J. Meng and Z. Li, *Adv. Opt. Mater.*, 2022, **10**, 2102468.

31 J. Huang, Q. Li, X. Lu, J. Meng and Z. Li, *Adv. Mater. Interfaces*, 2022, **9**, 2200327.

32 F. Duran, C. Diaz-Uribe, W. Vallejo, A. Muñoz-Acevedo, E. Schott and X. Zarate, *ACS Omega*, 2023, **8**, 27284–27292.

33 S. Tichapondwa, J. Newman and O. Kubheka, *Phys. Chem. Earth (Pt A, B, C)*, 2020, **118–119**, 102900.

34 G. Dubourg and M. Radović, *ACS Appl. Mater. Interfaces*, 2019, **11**, 6257–6266.

35 Z. Peng, Z. He, L. Li, L. Xiong and M. Fan, *Appl. Organomet. Chem.*, 2024, **38**, e7374.

36 J. Zhao, S. C. Nguyen, R. Ye, B. Ye, H. Weller, G. A. Somorjai, A. P. Alivisatos and F. D. Toste, *ACS Cent. Sci.*, 2017, **3**, 482–488.

37 M. Suwarnkar, R. Dhabbe, A. Kadam and K. Garadkar, *Ceram. Int.*, 2014, **40**, 5489–5496.

38 L. Ren, Y. Li, J. Hou, X. Zhao and C. Pan, *ACS Appl. Mater. Interfaces*, 2014, **6**, 1608–1615.

39 P. S. Khiabani, A. H. Soeriyadi, P. J. Reece and J. J. Gooding, *ACS Sens.*, 2016, **1**, 775–780.

40 R. Khayyam Nekouei, F. Pahlevani, M. Mayyas, S. Maroufi and V. Sahajwalla, *J. Environ. Chem. Eng.*, 2019, **7**, 103133.

41 I. L. Weatherall and B. D. Coombs, *J. Invest. Dermatol.*, 1992, **99**, 468–473.

42 D. Durmus, *Color Res. Appl.*, 2020, **45**, 796–802.

43 R. Daghrir, P. Drogui and D. Robert, *Ind. Eng. Chem. Res.*, 2013, **52**, 3581–3599.

44 U. Akpan and B. Hameed, *J. Hazard. Mater.*, 2009, **170**, 520–529.

45 P. N. Linnik and V. A. Zhezherya, *Russ. J. Gen. Chem.*, 2015, **85**, 2908–2920.

46 B. Chakraborty and I. A. Weinstock, *Coord. Chem. Rev.*, 2019, **382**, 85–102.

47 A. Monshi, M. R. Foroughi and M. R. Monshi, *World J. Nano Sci. Eng.*, 2012, **02**, 154–160.

48 Z. U. Abideen, J.-G. Choi, J. A. Yuwono, A. Kiy, P. V. Kumar, K. Murugappan, W.-J. Lee, P. Kluth, D. R. Nisbet, T. Tran-Phu, M. Yoon and A. Tricoli, *Adv. Electron. Mater.*, 2023, **9**, 2200905.

49 Z. U. Abideen, J.-G. Choi, J. A. Yuwono, W.-J. Lee, K. Murugappan, P. V. Kumar, D. R. Nisbet, T. Trãn-Phú, M.-H. Yoon and A. Tricoli, *ACS Appl. Mater. Interfaces*, 2023, **15**, 56464–56477.